



UNIVERSITY OF LEEDS

This is a repository copy of *An energy stable one-field monolithic arbitrary Lagrangian-Eulerian formulation for fluid-structure interaction*.

White Rose Research Online URL for this paper:
<https://eprints.whiterose.ac.uk/163737/>

Version: Accepted Version

Article:

Wang, Y orcid.org/0000-0002-5673-042X, Jimack, PK, Walkley, MA orcid.org/0000-0003-2541-4173 et al. (1 more author) (2020) An energy stable one-field monolithic arbitrary Lagrangian-Eulerian formulation for fluid-structure interaction. *Journal of Fluids and Structures*, 98. 103117. ISSN 0889-9746

<https://doi.org/10.1016/j.jfluidstructs.2020.103117>

© 2020, Elsevier. This manuscript version is made available under the CC-BY-NC-ND 4.0 license <http://creativecommons.org/licenses/by-nc-nd/4.0/>.

Reuse

Items deposited in White Rose Research Online are protected by copyright, with all rights reserved unless indicated otherwise. They may be downloaded and/or printed for private study, or other acts as permitted by national copyright laws. The publisher or other rights holders may allow further reproduction and re-use of the full text version. This is indicated by the licence information on the White Rose Research Online record for the item.

Takedown

If you consider content in White Rose Research Online to be in breach of UK law, please notify us by emailing eprints@whiterose.ac.uk including the URL of the record and the reason for the withdrawal request.



eprints@whiterose.ac.uk
<https://eprints.whiterose.ac.uk/>

1
2
3
4
5
6
7
8
9
10
11
12
13
14
15
16
17
18

An energy stable one-field monolithic arbitrary Lagrangian-Eulerian formulation for fluid-structure interaction

Yongxing Wang^{a,*}, Peter K. Jimack^b, Mark A. Walkley^b, Olivier Pironneau^c

^a*School of Mechanical Engineering, University of Leeds, Leeds, UK, LS2 9JT*

^b*School of Computing, University of Leeds, Leeds, UK, LS2 9JT*

^c*Laboratoire Jacques-Louis Lions, Sorbonne Universités, Paris, France*

Abstract

21
22
23
24
25
26
27
28
29
30
31
32
33
34

In this article we present a one-field monolithic finite element method in the Arbitrary Lagrangian-Eulerian (ALE) formulation for Fluid-Structure Interaction (FSI) problems. The method only solves for one velocity field in the whole FSI domain, and it solves in a monolithic manner so that the fluid solid interface conditions are satisfied automatically. We prove that the proposed scheme is unconditionally stable, through energy analysis, by utilising a conservative formulation and an exact quadrature rule. We implement the algorithm using both \mathbf{F} -scheme and \mathbf{d} -scheme, and demonstrate that the former has the same formulation in two and three dimensions. Finally several numerical examples are presented to validate this methodology, including combination with remesh techniques to handle the case of very large solid displacement.

Keywords: fluid structure interaction, finite element, one field, monolithic scheme, arbitrary Lagrangian-Eulerian, energy stable

1. Introduction

37
38
39
40
41
42
43
44
45
46

Numerical methods for Fluid-Structure Interaction (FSI) have been widely studied during the past decades, and a variety of methodologies have been developed in order to address different aspects of the FSI problem. However stability analyses of the existing numerical methods are rare especially when large solid deformation is involved. This paper is dedicated to developing a one-field monolithic FSI method in the Arbitrary Lagrangian-Eulerian (ALE) framework, and establishing its stability analysis over time.

47
48
49
50
51
52
53
54
55
56

Monolithic methods have been regarded as the most robust FSI algorithms in the literature [1–9], which solve for the fluid and solid variables simultaneously

*Corresponding author

Email address: scsywan@leeds.ac.uk/yongxingwang6@gmail.com (Yongxing Wang)

57
58
59
60
61
62
63
64
65
66
67
15 in one equation system. Among these methodologies for FSI problems, the one-
field approaches [6, 7, 9, 10] express the solid equation in terms of velocity, thus
only solve for one velocity in the whole FSI domain. In this case the whole
system can be solved similarly to a modified fluid problem, and the coupling
conditions at fluid and solid interface are automatically satisfied.

16
17
18
19
20
21
22
23
24
25
26
27
28
29
30
31
32
33
34
35
36
37
38
39
40
41
42
43
44
45
46
47
48
49
50
51
52
53
54
55
56
57
58
59
60
61
62
63
64
65
66
67
68
69
70
71
72
73
74
75
76
77
78
79
80
81
82
83
84
85
86
87
88
89
90
91
92
93
94
95
96
97
98
99
100
101
102
103
104
105
106
107
108
109
110
111
112

The stability analysis when using the ALE framework is challenging, even
for the pure fluid problem, due to the arbitrary moving frame [11–13]. [14, 15]
present an energy stable Fictitious Domain Method with Distributed Lagrangian
Multiplier (FDM/DLM), and [6, 16] present an energy stable Eulerian formu-
lation by remeshing. There is also some analysis on the existence and stability
of solutions of different FSI formulations, such as [17–20]. In a previous study
[8] we analysed the energy stability for a one-field FDM method. In this article
we extend this one-field idea to the ALE formulation, and the stability result
is achieved by expressing the fluid and solid equations in a conservative formu-
lation. In this sense, the formulation is similar to the one introduced in [6].
However it differs from [6] in the following perspectives: (1) we formulate the
solid in the reference domain and analyse the FSI problem in an ALE frame of
reference, in which case the formulation and analysis are exactly the same for two
and three dimensional cases, whereas [6] formulates and analyses everything in
the current domain, for which the three dimensional case is significantly more
complicated [21]; (2) we update the solid deformation tensor (the \mathbf{F} -scheme)
while [6] updates the solid displacement (the \mathbf{d} -scheme); (3) we implement the
scheme by solving an additional solid-like equation at each time step in order
to move the mesh, whilst [6] implements their scheme by remeshing which is
expensive in the three dimensional case.

The paper is organized as follows. In Section 2 the control equations for
the FSI problem are introduced in an ALE framework. In Section 3 the finite
element weak formulation is introduced, followed by spatial and time discretisa-
tions in Section 4. The main results of energy stability are presented in Section
5. Implementation details are considered in Section 6 and numerical examples
are given in Section 7, with some conclusions in Section 8.

2. The arbitrary Lagrangian-Eulerian description for the FSI problem

Let $\Omega_t^f \subset \mathbb{R}^d$ and $\Omega_t^s \subset \mathbb{R}^d$ be the fluid and solid domain respectively (which
are time dependent regions), $\Gamma_t = \overline{\Omega}_t^f \cap \overline{\Omega}_t^s$ is the moving interface between
the fluid and solid, and $\Omega_t = \overline{\Omega}_t^f \cup \overline{\Omega}_t^s$ has an outer boundary $\partial\Omega_t$, which can
be fixed or moving as shown in Figure 1. We use the superscripts f and s to
denote the fluid and solid variables respectively in the above and throughout
this article. The Eulerian description is convenient when we observe a fluid
from a fixed frame, while the Lagrangian description is convenient when we
observe a solid from a frame moving with it. An ALE frame of reference can be
adopted when a fluid and solid share an interface and interact with each other
as shown in Figure 1, in which case the frame moves arbitrarily from a reference
configuration Ω_{t_0} , chosen to be the same as the initial configuration at t_0 , to a

current configuration Ω_t . Let us define a family of mappings \mathcal{A}_t :

$$\mathcal{A}_t : \Omega_{t_0} \subset \mathbb{R}^d \rightarrow \Omega_t \subset \mathbb{R}^d, \quad (1)$$

with $d = 2, 3$ being the dimensions. We assume that $\mathcal{A}_t \in C^0(\overline{\Omega_{t_0}})^d$ is one-to-one and invertible with continuous inverse $\mathcal{A}_t^{-1} \in C^0(\overline{\Omega_t})^d$. Hence a point $\hat{\mathbf{x}} \in \Omega_{t_0}$ has a unique image $\mathbf{x} \in \Omega_t$ at time t , i.e.

$$\mathbf{x} = \mathcal{A}(\hat{\mathbf{x}}, t) = \mathcal{A}_t(\hat{\mathbf{x}}), \quad (2)$$

and a point $\mathbf{x} \in \Omega_t$ at time t has a unique inverse image $\hat{\mathbf{x}} \in \Omega_{t_0}$

$$\hat{\mathbf{x}} = \hat{\mathcal{A}}(\mathbf{x}, t) = \mathcal{A}_t^{-1}(\mathbf{x}). \quad (3)$$

We call $\mathbf{x} \in \Omega_t$ the Eulerian coordinate, and call its inverse image $\hat{\mathbf{x}}$, via the above mapping \mathcal{A}_t^{-1} , the ALE coordinate. We assume that $\mathcal{A}(\hat{\mathbf{x}}, t)$ is differentiable with respect to t for all $\hat{\mathbf{x}} \in \Omega_{t_0}$, and define the velocity of the ALE frame as

$$\mathbf{w}(\hat{\mathbf{x}}, t) = \frac{\partial \mathcal{A}}{\partial t}(\hat{\mathbf{x}}, t). \quad (4)$$

Given an Eulerian coordinate $\mathbf{x} \in \Omega_t$, its corresponding ALE coordinate $\hat{\mathbf{x}}_1 \in \Omega_{t_0}$ should be distinguished from its material (or Lagrangian) coordinate $\hat{\mathbf{x}}_2 \in \Omega_{t_0}$ as shown in Figure 1. In fact $\hat{\mathbf{x}}_2 \in \Omega_{t_0}$ (not necessarily the same as $\hat{\mathbf{x}}_1$) maps to $\mathbf{x} \in \Omega_t$ via the Lagrangian mapping, i.e., the trajectory of a material particle at $\hat{\mathbf{x}}_2$:

$$\mathcal{F}_t : \hat{\mathbf{x}} \mapsto \mathbf{x} = \mathcal{F}(\hat{\mathbf{x}}, t), \quad (5)$$

and the velocity of the material particle at $\hat{\mathbf{x}} \in \Omega_{t_0}$ is defined by

$$\mathbf{u}(\hat{\mathbf{x}}, t) = \frac{\partial \mathcal{F}}{\partial t}. \quad (6)$$

Remark 1. *Although the Lagrangian configuration and the ALE configuration are not generally the same, both are chosen to have the initial configuration Ω_{t_0} in this article. We shall also construct the ALE mapping such that $\mathcal{A}_t(\Omega_{t_0})$ coincides with $\mathcal{F}_t(\Omega_{t_0})$ at all boundaries including the fluid-solid interface: $\mathcal{A}_t(\partial\Omega_{t_0}) = \mathcal{F}_t(\partial\Omega_{t_0})$ and $\mathcal{A}_t(\Gamma_t) = \mathcal{F}_t(\Gamma_t)$.*

Remark 2. *The ALE mapping is the mapping that is actually used to move the domain in this article, and the purpose of introducing the Lagrangian mapping is to discuss its related variables, such as particle velocity \mathbf{u} and solid deformation tensor \mathbf{F} , which will be defined in the following context.*

Formulated in the current configuration, the conservation of momentum takes the same form in the fluid and solid domain Ω :

$$\rho \frac{d\mathbf{u}(\mathbf{x}, t)}{dt} = \text{div}(\boldsymbol{\sigma}) + \rho \mathbf{g}, \quad (7)$$

169
170
171
172
173
174
175
176
177
178
179
180
181
182
183
184
185
186
187
188
189
190
191
192
193
194
195
196
197
198
199
200
201
202
203
204
205
206
207
208
209
210
211
212
213
214
215
216
217
218
219
220
221
222
223
224

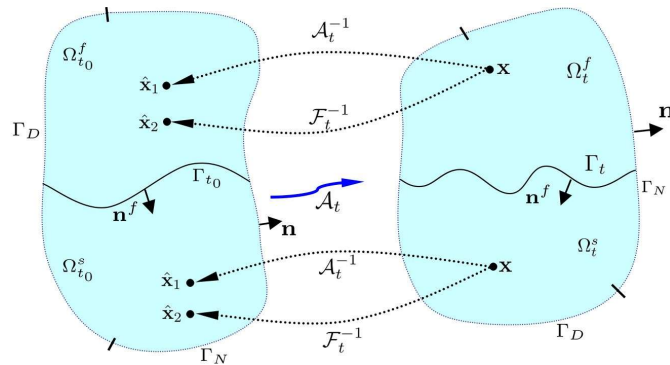


Figure 1: ALE mapping from Ω_{t_0} to Ω_t . Also shows the comparison between ALE mapping and Lagrangian mapping with Eulerian coordinate \mathbf{x} , ALE coordinate $\hat{\mathbf{x}}_1$ and material (Lagrangian) coordinate $\hat{\mathbf{x}}_2$. $\Gamma_t = \bar{\Omega}_t^f \cap \bar{\Omega}_t^s$ and $\Omega_t = \bar{\Omega}_t^f \cup \bar{\Omega}_t^s$, $\partial\Omega_t = \Gamma_D \cup \Gamma_N$.

with ρ , \mathbf{g} , \mathbf{u} and $\boldsymbol{\sigma}$ being the density, gravity acceleration, velocity and Cauchy stress tensor respectively. Here we use the notation $\rho = \begin{cases} \rho^f & \text{in } \Omega_t^f \\ \rho^s & \text{in } \Omega_t^s \end{cases}$, with the superscript f and s denote fluid and solid respectively, and similar notations are also applied to \mathbf{u} and $\boldsymbol{\sigma}$. In the above, $\frac{d(\cdot)}{dt}$ is the total derivative computed along the trajectory of a material particle at \mathbf{x} , i.e. via the Lagrangian mapping:

$$\frac{d\mathbf{u}(\mathbf{x}, t)}{dt} = \frac{d\mathbf{u}(\mathcal{F}_t(\hat{\mathbf{x}}), t)}{dt} = \frac{\partial \mathbf{u}}{\partial t} \Big|_{\mathbf{x}=\mathcal{F}(\hat{\mathbf{x}}, t)} + (\mathbf{u} \cdot \nabla) \mathbf{u}. \quad (8)$$

Replacing the above partial time derivative by the total derivative of

$$\frac{d\mathbf{u}(\mathcal{A}_t(\hat{\mathbf{x}}), t)}{dt} = \frac{\partial \mathbf{u}}{\partial t} \Big|_{\mathbf{x}=\mathcal{A}(\hat{\mathbf{x}}, t)} + (\mathbf{w} \cdot \nabla) \mathbf{u} \quad (9)$$

leads to the ALE formulation of (7)

$$\rho \frac{d\mathbf{u}(\mathcal{A}_t(\hat{\mathbf{x}}), t)}{dt} + \rho((\mathbf{u} - \mathbf{w}) \cdot \nabla) \mathbf{u} = \text{div}(\boldsymbol{\sigma}) + \rho \mathbf{g} \quad \text{in } \Omega. \quad (10)$$

We consider here both an incompressible fluid and incompressible solid:

$$\boldsymbol{\sigma} = \boldsymbol{\tau} - p\mathbf{I}, \quad (11)$$

with $\boldsymbol{\tau}$ being the deviatoric part of the stress tensor. For a Newtonian fluid in Ω_t^f ,

$$\boldsymbol{\tau} = \boldsymbol{\tau}^f = \mu^f \mathbf{D}\mathbf{u} = \mu^f (\nabla \mathbf{u} + \nabla^T \mathbf{u}), \quad (12)$$

and for a hyperelastic solid [22] in Ω_t^s ,

$$\boldsymbol{\tau} = \boldsymbol{\tau}^s = J_{\mathcal{F}_t}^{-1} \frac{\partial \Psi(\mathbf{F})}{\partial \mathbf{F}} \mathbf{F}^T, \quad (13)$$

with

$$\mathbf{F} = \frac{\partial \mathcal{F}(\hat{\mathbf{x}}, t)}{\partial \hat{\mathbf{x}}} \quad (14)$$

being the deformation tensor of the solid, $J_{\mathcal{F}_t}$ being the determinant of \mathbf{F} , and $\Psi(\mathbf{F})$ being the energy function of the hyperelastic solid material. Combining with the continuity equation

$$\nabla \cdot \mathbf{u} = 0 \quad \text{in } \Omega_t, \quad (15)$$

the FSI system is completed with continuity of the velocity and normal stress conditions on the interface Γ_t :

$$\mathbf{u}^f = \mathbf{u}^s, \quad \boldsymbol{\sigma}^f \mathbf{n}^f = \boldsymbol{\sigma}^s \mathbf{n}^f, \quad (16)$$

and (for simplicity of this exposition) homogeneous Dirichlet and Neumann boundaries on Γ_D and Γ_N respectively:

$$\mathbf{u} = 0, \quad \boldsymbol{\sigma} \mathbf{n} = 0, \quad (17)$$

with $\Gamma_D \cup \Gamma_N = \partial\Omega_t$ as shown in Figure 1.

3. Finite element weak formulation

Let $L^2(\omega)$ be the square integrable functions in domain ω , endowed with norm $\|u\|_{0,\omega}^2 = \int_{\omega} |u|^2$. Let $H^1(\omega) = \{u : u \in L^2(\omega), \nabla u \in L^2(\omega)^d\}$ with the norm denoted by $\|u\|_{1,\omega}^2 = \|u\|_{0,\omega}^2 + \|\nabla u\|_{0,\omega}^2$. We also denote by $H_0^1(\omega)$ the subspace of $H^1(\omega)$ whose functions have zero value on the Dirichlet boundary of ω .

According to equation (2) we construct Ω_t from Ω_{t_0} , so a function $v \in H_0^1(\Omega_t)$ is one-to-one corresponding to a function $\hat{v} \in H_0^1(\Omega_{t_0})$ via

$$v \circ \mathcal{A}_t = \hat{v}. \quad (18)$$

Choosing a test function $\mathbf{v}(\mathbf{x}) = \mathbf{v} \circ \mathcal{A}_t(\hat{\mathbf{x}}) = \hat{\mathbf{v}}(\hat{\mathbf{x}})$, the weak formulation may be obtained by multiplying \mathbf{v} on both sides of equation (10), and integrating the stress term by parts in domain Ω_t^f and Ω_t^s separately:

$$\begin{aligned} & \rho^f \int_{\Omega_t^f} \frac{d\mathbf{u}(\mathcal{A}_t(\hat{\mathbf{x}}), t)}{dt} \cdot \mathbf{v} + \rho^f \int_{\Omega_t^f} ((\mathbf{u} - \mathbf{w}) \cdot \nabla) \mathbf{u} \cdot \mathbf{v} \\ & + \frac{\mu^f}{2} \int_{\Omega_t^f} \mathbf{D}\mathbf{u} : \mathbf{D}\mathbf{v} - \int_{\Omega_t^f} p \nabla \cdot \mathbf{v} = \int_{\partial\Omega_t^f} \boldsymbol{\sigma}^f \mathbf{n}^f \cdot \mathbf{v} + \rho^f \int_{\Omega_t^f} \mathbf{g} \cdot \mathbf{v}. \end{aligned} \quad (19)$$

$$\begin{aligned} & \rho^s \int_{\Omega_t^s} \frac{d\mathbf{u}(\mathcal{A}_t(\hat{\mathbf{x}}), t)}{dt} \cdot \mathbf{v} + \rho^s \int_{\Omega_t^s} ((\mathbf{u} - \mathbf{w}) \cdot \nabla) \mathbf{u} \cdot \mathbf{v} \\ & + \int_{\Omega_{t_0}^s} \frac{\partial \Psi}{\partial \mathbf{F}} : \nabla_{\hat{\mathbf{x}}} \mathbf{v} - \int_{\Omega_t^s} p \nabla \cdot \mathbf{v} = \int_{\partial\Omega_t^s} \boldsymbol{\sigma}^s (-\mathbf{n}^f) \cdot \mathbf{v} + \rho^s \int_{\Omega_t^s} \mathbf{g} \cdot \mathbf{v}. \end{aligned} \quad (20)$$

We used $\frac{\partial \Psi}{\partial \mathbf{F}} \mathbf{F}^T : \nabla \mathbf{v} = \frac{\partial \Psi}{\partial \mathbf{F}} : \nabla \mathbf{v} \mathbf{F} = \frac{\partial \Psi}{\partial \mathbf{F}} : \nabla_{\hat{\mathbf{x}}} \mathbf{v}$ in the above deduction. Using the interface and boundary conditions (16) and (17), we have the following equation by adding up (19) and (20).

$$\begin{aligned} & \rho \int_{\Omega_t} \frac{d\mathbf{u}(\mathcal{A}_t(\hat{\mathbf{x}}), t)}{dt} \cdot \mathbf{v} + \rho \int_{\Omega_t} ((\mathbf{u} - \mathbf{w}) \cdot \nabla) \mathbf{u} \cdot \mathbf{v} \\ & + \frac{\mu^f}{2} \int_{\Omega_t^f} \mathbf{D}\mathbf{u} : \mathbf{D}\mathbf{v} - \int_{\Omega_t} p \nabla \cdot \mathbf{v} + \int_{\Omega_{t_0}^s} \frac{\partial \Psi}{\partial \mathbf{F}} : \nabla_{\hat{\mathbf{x}}} \mathbf{v} = \rho \int_{\Omega_t} \mathbf{g} \cdot \mathbf{v}. \end{aligned} \quad (21)$$

Using Jacobi's formula [23], we have

$$\begin{aligned} \frac{\partial J_{\mathcal{A}_t}}{\partial t} &= \text{trace} \left(J_{\mathcal{A}_t} \mathbf{A}^{-1} \frac{\partial \mathbf{A}}{\partial t} \right) \\ &= \text{trace} \left(J_{\mathcal{A}_t} \mathbf{A}^{-1} \nabla_{\hat{\mathbf{x}}} \frac{\partial \mathcal{A}_t}{\partial t} \right) \\ &= J_{\mathcal{A}_t} \nabla \cdot \frac{\partial \mathcal{A}_t}{\partial t} = J_{\mathcal{A}_t} \nabla \cdot \mathbf{w}, \end{aligned} \quad (22)$$

with $\mathbf{A} = \frac{\partial \mathcal{A}(\hat{\mathbf{x}}, t)}{\partial \hat{\mathbf{x}}} = \nabla_{\hat{\mathbf{x}}} \mathcal{A}_t$. Then we can take the time derivative outside the moving domain (conservative formulation [11]),

$$\begin{aligned} \frac{d}{dt} \int_{\Omega_t} \mathbf{u}(\mathbf{x}, t) \cdot \mathbf{v}(\mathbf{x}) &= \frac{d}{dt} \int_{\Omega_{t_0}} J_{\mathcal{A}_t} \mathbf{u}(\mathcal{A}_t(\hat{\mathbf{x}}), t) \cdot \hat{\mathbf{v}}(\hat{\mathbf{x}}) \\ &= \int_{\Omega_t} \frac{d\mathbf{u}(\mathbf{x}, t)}{dt} \cdot \mathbf{v}(\mathbf{x}) + \int_{\Omega_t} (\nabla \cdot \mathbf{w}) \mathbf{u}(\mathbf{x}, t) \cdot \mathbf{v}(\mathbf{x}). \end{aligned} \quad (23)$$

Substituting (23) into (21), using

$$\text{div}(\mathbf{w} \otimes \mathbf{u}) = (\mathbf{w} \cdot \nabla) \mathbf{u} + (\nabla \cdot \mathbf{w}) \mathbf{u}, \quad (24)$$

and combining the weak form of continuity equation (15), leads to the weak formulation of the FSI problem:

Problem 1. Given Ω_{t_0} , Γ_{t_0} , $\mathbf{u}(\hat{\mathbf{x}}, t_0)$ and an ALE mapping \mathcal{A}_t (consequently given \mathbf{w} by (4)), $\forall \hat{\mathbf{x}} \in \Omega_{t_0} : \forall t \in (0, T]$ find $\mathbf{u}(\mathbf{x}, t) = \mathbf{u}(\mathcal{A}_t(\hat{\mathbf{x}}), t) \in H_0^1(\Omega_t)^d$ and $p(\mathbf{x}, t) = p(\mathcal{A}_t(\hat{\mathbf{x}}), t) \in L^2(\Omega_t)$, such that $\forall \mathbf{v}(\mathbf{x}) = \mathbf{v}(\mathcal{A}_t(\hat{\mathbf{x}}))$, $\mathbf{v} \in H_0^1(\Omega_t)^d$ and $\forall q(\mathbf{x}) = q(\mathcal{A}_t(\hat{\mathbf{x}}))$, $q \in L^2(\Omega_t)$, the following equations hold:

$$\begin{aligned} & \rho \frac{d}{dt} \int_{\Omega_t} \mathbf{u}(\mathcal{A}_t(\hat{\mathbf{x}}), t) \cdot \mathbf{v} + \rho \int_{\Omega_t} (\mathbf{u} \cdot \nabla) \mathbf{u} \cdot \mathbf{v} + \rho \int_{\Omega_t} (\mathbf{w} \otimes \mathbf{u}) : \nabla \mathbf{v} \\ & + \frac{\mu^f}{2} \int_{\Omega_t^f} \mathbf{D}\mathbf{u} : \mathbf{D}\mathbf{v} - \int_{\Omega_t} p \nabla \cdot \mathbf{v} + \int_{\Omega_{t_0}^s} \frac{\partial \Psi}{\partial \mathbf{F}}(\mathbf{F}) : \nabla_{\hat{\mathbf{x}}} \mathbf{v} = \rho \int_{\Omega_t} \mathbf{g} \cdot \mathbf{v}, \end{aligned} \quad (25)$$

$$- \int_{\Omega_t} q \nabla \cdot \mathbf{u} = 0, \quad (26)$$

and

$$\mathcal{A}_t(\partial\Omega_{t_0}) = \mathcal{F}_t(\partial\Omega_{t_0}), \quad \mathcal{A}_t(\Gamma_{t_0}) = \mathcal{F}_t(\Gamma_{t_0}), \quad (27)$$

with Γ_{t_0} and $\partial\Omega_{t_0}$ being the initial interface and outer boundary respectively, as shown in Figure 1, and \mathcal{F}_t being the Lagrangian mapping as defined in (5).

4. Discretisation in space and time

Define a stable finite element space, such as the Taylor-Hood elements, for the velocity-pressure pair (\mathbf{u}, p) in Ω_{t_0} :

$$V^h(\Omega_{t_0}) = \text{span} \{ \hat{\varphi}_1, \dots, \hat{\varphi}_{N^u} \} \subset H_0^1(\Omega_{t_0})$$

and

$$L^h(\Omega_{t_0}) = \text{span} \{ \hat{\phi}_1, \dots, \hat{\phi}_{N^p} \} \subset L^2(\Omega_{t_0}),$$

with N^u and N^p being the number of nodal variables for each velocity component and pressure respectively. Then

$$V^h(\Omega_t) = \{ \varphi_h : \varphi_h = \hat{\varphi}_h \circ \mathcal{A}_t^{-1}, \hat{\varphi}_h \in V^h(\Omega_{t_0}) \},$$

and

$$L^h(\Omega_t) = \{ \phi_h : \phi_h = \hat{\phi}_h \circ \mathcal{A}_t^{-1}, \hat{\phi}_h \in L^h(\Omega_{t_0}) \}.$$

Using the backward Euler scheme, equation (25) and (26) can be discretised respectively as follows:

$$\begin{aligned} & \frac{\rho}{\delta t} \int_{\Omega_{t_{n+1}}} \mathbf{u}_{n+1}^h \cdot \mathbf{v} - \frac{\rho}{\delta t} \int_{\Omega_{t_n}} \mathbf{u}_n^h \cdot \mathbf{v} + \rho \int_{\Omega_{t_{n+1}}} (\mathbf{u}_{n+1}^h \cdot \nabla) \mathbf{u}_{n+1}^h \cdot \mathbf{v} \\ & + \rho \mathcal{I}(\xi(\tau)) + \frac{\mu^f}{2} \int_{\Omega_{t_{n+1}}^f} \text{D}\mathbf{u}_{n+1}^h : \text{D}\mathbf{v} - \int_{\Omega_{t_{n+1}}} p_{n+1}^h \nabla \cdot \mathbf{v} \\ & + \int_{\Omega_{t_0}^s} \frac{\partial \Psi}{\partial \mathbf{F}}(\mathbf{F}_{n+1}) : \nabla_{\mathbf{x}} \mathbf{v} = \int_{\Omega_{t_{n+1}}} \rho \mathbf{g} \cdot \mathbf{v}, \end{aligned} \quad (28)$$

and

$$- \int_{\Omega_{t_{n+1}}} q \nabla \cdot \mathbf{u}_{n+1}^h = 0. \quad (29)$$

In the above

$$\xi(\tau) = \int_{\Omega_\tau} (\mathbf{w}(\tau) \otimes \mathbf{u}_{n+1}^h) : \nabla \mathbf{v}, \quad (30)$$

and $\delta t \mathcal{I}(\xi)$ is a quadrature formula used to compute $\int_{t_n}^{t_{n+1}} \xi(\tau)$. In order to have an unconditionally stable scheme, which will be proved in Section 5, the mid-point integration is adopted for this term, i.e.:

$$\mathcal{I}(\xi) = \xi(t_{n+1/2}) \quad (31)$$

in the two dimensional case, and the Simpson formula is adopted in the three dimensional case:

$$\mathcal{I}(\xi) = \frac{2}{3} \xi(t_{n+1/2}) + \frac{1}{6} \xi(t_n) + \frac{1}{6} \xi(t_{n+1}). \quad (32)$$

393
394
395
396
397
398
399
400
401
402
403
404
405
406
407
408
409
410
411
412
413
414
415
416
417
418
419
420
421
422
423
424
425
426
427
428
429
430
431
432
433
434
435
436
437
438
439
440
441
442
443
444
445
446
447
448

Notice that the Simpson formula can also be adopted in the two dimensional case, but the mid-point rule is simpler (and still of the same order as the temporal discretisation). Due to the definition of the deformation tensor \mathbf{F} (14) and ALE velocity \mathbf{w} (4), we have

$$\frac{\mathbf{F}_{n+1} - \mathbf{F}_n}{\delta t} = \frac{\mathbf{F}_{n+1} \circ \mathcal{F}_{t_{n+1}}(\hat{\mathbf{x}}) - \mathbf{F}_n \circ \mathcal{F}_{t_n}(\hat{\mathbf{x}})}{\delta t} \approx \nabla_{\hat{\mathbf{x}}} \mathbf{u}_{n+1}, \quad (33)$$

and

$$\frac{\mathbf{x}_{n+1} - \mathbf{x}_n}{\delta t} = \frac{\mathcal{A}_{t_{n+1}}(\hat{\mathbf{x}}) - \mathcal{A}_{t_n}(\hat{\mathbf{x}})}{\delta t} \approx \mathbf{w}_{n+1}. \quad (34)$$

Therefore \mathbf{F}_{n+1} and $\Omega_{t_{n+1}}$ in (28) can be updated as follows:

$$\mathbf{F}_{n+1} = \mathbf{F}_n + \delta t \nabla_{\hat{\mathbf{x}}} \mathbf{u}_{n+1}, \quad (35)$$

and

$$\Omega_{t_{n+1}} = \mathcal{A}_{t_{n+1}}(\Omega_{t_0}) = \{\mathbf{x} : \mathbf{x} = \mathbf{x}_n + \delta t \mathbf{w}_{n+1}, \mathbf{x}_n \in \mathcal{A}_{t_n}(\Omega_{t_0})\}. \quad (36)$$

65 Up to now we have not stated how to construct \mathbf{w} (or \mathcal{A}_t), because very often we only need to construct the ALE mapping \mathcal{A}_t at a discrete time level, that is to say computing $\mathcal{A}_{t_{n+1}}$ for $n = 0, 1, \dots$ at each time step. This will be explained in the rest of this section.

We solve the following static linear elastic equation in $\Omega_{t_{n+1}}$ in order to 70 compute \mathbf{w}_{n+1} , and take $\mathbf{w}(t) = \mathbf{w}_{n+1}$ for $t \in (t_n, t_{n+1}]$. Given the following boundary data:

$$\mathbf{w}_{n+1} \cdot \mathbf{n} = 0, \quad \mathbf{n} \cdot \mathbf{D}\mathbf{w}_{n+1} \cdot \mathbf{t} = 0 \quad \text{on} \quad \partial\Omega_{t_{n+1}}, \quad (37)$$

and

$$\mathbf{w}_{n+1} = \mathbf{u}_{n+1}^h \quad \text{on} \quad \Gamma_{t_{n+1}}, \quad (38)$$

find $\mathbf{w}_{n+1} \in V^h(\Omega_{t_{n+1}})^d$ such that $\forall \mathbf{z} \in V^h(\Omega_{t_{n+1}})^d$, the following equation holds:

$$\frac{\mu}{2} \int_{\Omega_{t_{n+1}}} \mathbf{D}\mathbf{w}_{n+1} : \mathbf{D}\mathbf{z} + \lambda \int_{\Omega_{t_{n+1}}} (\nabla \cdot \mathbf{w}_{n+1}) (\nabla \cdot \mathbf{z}) = 0, \quad (39)$$

with μ and λ being the Lamé constants used here as pseudo-solid parameters, which may be different from the solid parameters [24]. It is well known that the above elliptic problem (37) to (39) has a unique solution $\mathbf{w} \in V^h(\Omega_{t_{n+1}})$ [25] (notice that $\mathbf{n} \cdot \mathbf{D}\mathbf{w}_{n+1} \cdot \mathbf{t} = 0$ on $\partial\Omega_{t_{n+1}}$ should be enforced for the corresponding PDE equation of (39), with \mathbf{t} being the tangential direction of $\partial\Omega_{t_{n+1}}$). As a result, we are able to construct a mapping for $t \in (t_n, t_{n+1}]$,

$$\mathcal{A}_{t_n, t} : \Omega_{t_n} \rightarrow \Omega_t, \quad \mathcal{A}_{t_n, t}(\mathbf{x}_n) = \mathbf{x}_n + (t - t_n)\mathbf{w}_{n+1}, \quad (40)$$

and further

$$\mathcal{A}_t = \mathcal{A}_{t_0, t_1}^{-1} \circ \mathcal{A}_{t_1, t_2}^{-1} \cdots \circ \mathcal{A}_{t_n, t}^{-1}. \quad (41)$$

From the computational point of view, knowing the ALE velocity \mathbf{w}_{n+1} at the discrete level is sufficient.

Putting all the above together, the discrete ALE-FSI problem reads:

Problem 2. Given \mathcal{A}_{t_n} and $\mathbf{u}_n^h = \mathbf{u}(\mathcal{A}_{t_n}(\hat{\mathbf{x}}), t_n)$, $\forall \hat{\mathbf{x}} \in \Omega_{t_0}$ find $\mathbf{u}_{n+1}^h = \mathbf{u}(\mathcal{A}_{t_{n+1}}(\hat{\mathbf{x}}), t_{n+1}) \in V^h(\Omega_{t_{n+1}})^d$, $p_{n+1}^h = p(\mathcal{A}_{t_{n+1}}(\hat{\mathbf{x}}), t_{n+1}) \in L^h(\Omega_{t_{n+1}})$, and $\mathbf{w}_{n+1} \in V^h(\Omega_{t_{n+1}})^d$ (consequently an ALE mapping $\mathcal{A}_{t_{n+1}}$ by (41)), such that $\forall \mathbf{v}(\mathbf{x}) = \mathbf{v}(\mathcal{A}_{t_{n+1}}(\hat{\mathbf{x}}))$, $\mathbf{v} \in V^h(\Omega_{t_{n+1}})^d$, $\forall q(\mathbf{x}) = q(\mathcal{A}_{t_{n+1}}(\hat{\mathbf{x}}))$, $q \in L^h(\Omega_{t_{n+1}})$ and $\forall \mathbf{z} \in V^h(\Omega_{t_{n+1}})^d$, the following equation system holds:

$$\begin{aligned}
& \frac{\rho}{\delta t} \int_{\Omega_{t_{n+1}}} \mathbf{u}_{n+1}^h \cdot \mathbf{v} - \frac{\rho}{\delta t} \int_{\Omega_{t_n}} \mathbf{u}_n^h \cdot \mathbf{v} + \rho \int_{\Omega_{t_{n+1}}} (\mathbf{u}_{n+1}^h \cdot \nabla) \mathbf{u}_{n+1}^h \cdot \mathbf{v} \\
& + \rho \mathcal{I}(\xi(\tau)) + \frac{\mu^f}{2} \int_{\Omega_{t_{n+1}}^f} \mathbf{D}\mathbf{u}_{n+1}^h : \mathbf{D}\mathbf{v} - \int_{\Omega_{t_{n+1}}} p_{n+1}^h \nabla \cdot \mathbf{v} \\
& - \int_{\Omega_{t_{n+1}}} q \nabla \cdot \mathbf{u}_{n+1}^h + \int_{\Omega_{t_0}^s} \frac{\partial \Psi}{\partial \mathbf{F}}(\mathbf{F}_{n+1}) : \nabla_{\hat{\mathbf{x}}}\mathbf{v} \\
& + \frac{\mu}{2} \int_{\Omega_{t_{n+1}}} \mathbf{D}\mathbf{w}_{n+1} : \mathbf{D}\mathbf{z} + \lambda \int_{\Omega_{t_{n+1}}} (\nabla \cdot \mathbf{w}_{n+1}) (\nabla \cdot \mathbf{z}) = \int_{\Omega_{t_{n+1}}} \rho \mathbf{g} \cdot \mathbf{v}.
\end{aligned} \tag{42}$$

75 with quadrature formula (31) in 2D or (32) in 3D, updating \mathbf{F}_{n+1} by (35) and
 76 updating $\Omega_{t_{n+1}}$ by (36). In addition, the above FSI system equations are com-
 77 pleted with the Dirichlet and Neumann boundary conditions (17) for the momen-
 78 tum and continuity equations (28) and (29), and with the boundary conditions
 79 (37) and (38) for the mesh equation (39).

80 Problem 2 is a highly non-linear system, so we solve it iteratively as described
 in the following Algorithm 1.

Algorithm 1 Solve Problem 2 for $\mathcal{A}_{t_{n+1}}$ (or \mathbf{w}_{n+1}^h), \mathbf{u}_{n+1}^h and p_{n+1}^h

Require: $\Omega_{t_n} = \mathcal{A}_{t_n}(\Omega_{t_0})$, \mathbf{u}_n^h and a tolerance tol

Ensure: $\Omega_{t_{n+1}}^0 = \Omega_{t_n}$, $\mathbf{u}_{n+1}^0 = \mathbf{u}_n^h$ and $k = 0$

repeat

1. solve the mesh equation (39) for \mathbf{w}_{n+1}^{k+1} in $\Omega_{t_{n+1}}^k$ using boundary condi-
 tions (37) and (38) with \mathbf{u}_{n+1}^k
2. update $\Omega_{t_{n+1}}^{k+1} = \Omega_{t_{n+1}}^k + \delta t \mathbf{w}_{n+1}^{k+1}$ using (36)
3. solve the FSI system (28) and (29) in $\Omega_{t_{n+1}}^{k+1}$ for \mathbf{u}_{n+1}^{k+1} and p_{n+1}^{k+1}
4. $\epsilon_k = \frac{\|\mathbf{u}_{n+1}^{k+1} - \mathbf{u}_{n+1}^k\|}{\|\mathbf{u}_{n+1}^k\|}$, $k \leftarrow k + 1$

until $\epsilon_k < tol$

Remark 3. The mesh equation (39) is discretised as a positive definite linear
 equation system, and we solve it efficiently using a preconditioned Conjugate
 Gradient (pCG) method [26]. The FSI equations (28) and (29) are discretised
 85 as a saddle-point equation system. We use an operator splitting method and ef-
 ficiently solve a convection and Stokes problem separately [7, 27]. We solve the
 convection equation using pCG and the Stokes equation using a preconditioned

505
506
507
508
509
510
511
512
513
514
515
516
517
518
519
520
521
522
523
524
525
526
527
528
529
530
531
532
533
534
535
536
537
538
539
540
541
542
543
544
545
546
547
548
549
550
551
552
553
554
555
556
557
558
559
560

MinRes algorithm. The preconditioner for CG is an incomplete Cholesky decomposition of the system matrix, and the preconditioner of MinRes is an incomplete Cholesky decomposition of a modified system matrix, where the pressure mass matrix replaces the zero pressure block [28].

5. Stability analysis

We shall deduce an energy stability result for Problem 2 at the end of this section. In preparation for this we first prove the following lemmas.

Lemma 1. *If $(\mathbf{u}, p, \mathbf{w})$ is the solution of Problem 2, then \mathbf{u} satisfies the following at $t = t_{n+1}$.*

$$\int_{\Omega_t} (\mathbf{u} \cdot \nabla) \mathbf{u} \cdot \mathbf{u} = 0. \quad (43)$$

Proof. Noticing that

$$\int_{\Omega_t} (\mathbf{u} \cdot \nabla) \mathbf{u} \cdot \mathbf{u} = \int_{\Omega_t} \nabla \cdot (\mathbf{u} \otimes \mathbf{u}) \cdot \mathbf{u} - \int_{\Omega_t} |\mathbf{u}|^2 \nabla \cdot \mathbf{u}, \quad (44)$$

and integrating by parts:

$$\begin{aligned} \int_{\Omega_t} (\mathbf{u} \cdot \nabla) \mathbf{u} \cdot \mathbf{u} &= \int_{\partial\Omega_t} |\mathbf{u}|^2 \mathbf{u} \cdot \mathbf{n} - \int_{\Omega_t} (\mathbf{u} \cdot \nabla) \mathbf{u} \cdot \mathbf{u} - \int_{\Omega_t} |\mathbf{u}|^2 \nabla \cdot \mathbf{u}. \\ \Rightarrow \int_{\Omega_t} (\mathbf{u} \cdot \nabla) \mathbf{u} \cdot \mathbf{u} &= \frac{1}{2} \int_{\partial\Omega_t} |\mathbf{u}|^2 \mathbf{u} \cdot \mathbf{n} - \frac{1}{2} \int_{\Omega_t} |\mathbf{u}|^2 \nabla \cdot \mathbf{u}. \end{aligned} \quad (45)$$

⁹⁵ In the above $\int_{\partial\Omega_t} |\mathbf{u}|^2 \mathbf{u} \cdot \mathbf{n} = 0$, thanks to the enclosed flow $\mathbf{u} \cdot \mathbf{n} = 0$ (17). Using the Sobolev imbedding theorem [29, Theorem 6 in Chapter 5], we have $H^1 \subset L^\infty$ in the two dimensional case and $H^1 \subset L^6$ in the three dimensional case. Either L^∞ or L^6 is included in L^4 because Ω_t has finite measure. Therefore $\mathbf{u} \in H^1 \subset L^4 \Rightarrow |\mathbf{u}|^2 \in L^2$, and $\int_{\Omega_t} |\mathbf{u}|^2 \nabla \cdot \mathbf{u} = 0$ thanks to (29). \square

Lemma 2. *If $(\mathbf{u}, p, \mathbf{w})$ is the solution of Problem 2 then, for any $\mathbf{w} \in V^h(\Omega_t)$, \mathbf{u} satisfies the following at $t = t_{n+1}$.*

$$\xi(t) \equiv \int_{\Omega_t} (\mathbf{w} \otimes \mathbf{u}) : \nabla \mathbf{u} = -\frac{1}{2} \int_{\Omega_t} |\mathbf{u}|^2 \nabla \cdot \mathbf{w}. \quad (46)$$

Proof. Integrating by parts we get

$$\xi(t) = \int_{\partial\Omega_t} (\mathbf{w} \otimes \mathbf{u}) \mathbf{u} \cdot \mathbf{n} - \int_{\Omega_t} \nabla \cdot (\mathbf{w} \otimes \mathbf{u}) \cdot \mathbf{u} \quad (47)$$

The boundary integral in (47) is zero due to the enclosed flow $\mathbf{u} \cdot \mathbf{n} = 0$ condition (17). The second term on the right-hand side of (47) can be expressed as:

$$\int_{\Omega_t} \nabla \cdot (\mathbf{w} \otimes \mathbf{u}) \cdot \mathbf{u} = \xi(t) + \int_{\Omega_t} |\mathbf{u}|^2 \nabla \cdot \mathbf{w}, \quad (48)$$

¹⁰⁰ we then have (46) by substituting (48) into (47). \square

561
562
563
564
565
566
567
568
569
570
571
572
573
574
575
576
577
578
579
580
581
582
583
584
585
586
587
588
589
590
591
592
593
594
595
596
597
598
599
600
601
602
603
604
605
606
607
608
609
610
611
612
613
614
615
616

Lemma 3. *If $(\mathbf{u}_{n+1}, p_{n+1}, \mathbf{w}_{n+1})$ is the solution of Problem 2, then*

$$\|\mathbf{u}_{n+1}\|_{0, \Omega_{t_{n+1}}}^2 - \|\mathbf{u}_{n+1}\|_{0, \Omega_{t_n}}^2 = \delta t \mathcal{I}(\eta), \quad (49)$$

with

$$\eta(t) = \int_{\Omega_t} |\mathbf{u}_{n+1}|^2 \nabla \cdot \mathbf{w}(t), \quad t \in (t_n, t_{n+1}). \quad (50)$$

Proof. Since

$$\begin{aligned} \eta(t) &= \int_{\Omega_{t_n}} J_{\mathcal{A}_{t_n, t}} |\mathbf{u}_{n+1}|^2 \left(\frac{\partial \mathcal{A}_{t_n, t}^{-1}}{\partial \mathbf{x}} \nabla_{\mathbf{x}_n} \right) \cdot \mathbf{w}(t) \\ &= \int_{\Omega_{t_n}} |\mathbf{u}_{n+1}|^2 (\mathbf{C}_{\mathcal{A}_{t_n, t}} \nabla_{\mathbf{x}_n}) \cdot \mathbf{w}(t), \end{aligned} \quad (51)$$

where $\mathbf{C}_{\mathcal{A}_{t_n, t}}$ is the cofactor matrix of $\frac{\partial \mathcal{A}_{t_n, t}}{\partial \mathbf{x}}$. According to the way we construct $\mathcal{A}_{t_n, t}$ (40), we know $\mathbf{C}_{\mathcal{A}_{t_n, t}}$ is a polynomial in time of degree $d - 1$ [11], with $d = 2, 3$ being the space dimension. Also $\mathbf{w}(t) = \mathbf{w}_{n+1}$ is a constant for $t \in (t_n, t_{n+1}]$, so $\eta(t)$ is linear in time when $d = 2$ and quadratic when $d = 3$, and a mid-point integration ($d = 2$) or Simpson formula ($d = 3$) would exactly compute $\int_{t_n}^{t_{n+1}} \eta(t)$. This is to say

$$\mathcal{I}(\eta) = \int_{t_n}^{t_{n+1}} \eta(t). \quad (52)$$

Noticing that for $t \in (t_n, t_{n+1})$,

$$\begin{aligned} \frac{d}{dt} \int_{\Omega_t} |\mathbf{u}_{n+1}|^2 &= \frac{d}{dt} \int_{\Omega_{t_n}} J_{\mathcal{A}_{t_n, t}} |\mathbf{u}_{n+1}|^2 \\ &= \int_{\Omega_{t_n}} J_{\mathcal{A}_{t_n, t}} |\mathbf{u}_{n+1}|^2 \nabla_{\mathbf{x}} \mathbf{w}(t) = \eta(t), \end{aligned} \quad (53)$$

and using (52), we finally have (49). \square

Lemma 4. *Define potential energy of the solid:*

$$E(t) = \int_{\Omega_{t_0}^s} \Psi(\mathbf{F}). \quad (54)$$

If $(\mathbf{u}_{n+1}, p_{n+1}, \mathbf{w}_{n+1})$ is the solution of Problem 2 and $\Psi(\mathbf{F})$ is C^1 convex on the set of second order tensors [14], then

$$\delta t \int_{\Omega_{t_0}^s} \frac{\partial \Psi}{\partial \mathbf{F}}(\mathbf{F}_{n+1}) : \nabla_{\hat{\mathbf{x}}} \mathbf{u}_{n+1} \geq E(t_{n+1}) - E(t_n). \quad (55)$$

617
618
619
620
621
622
623
624
625
626
627
628
629
630
631
632
633
634
635
636
637
638
639
640
641
642
643
644
645
646
647
648
649
650
651
652
653
654
655
656
657
658
659
660
661
662
663
664
665
666
667
668
669
670
671
672

Proof. Let

$$w(t) = \Psi(\mathbf{F}_n + t(\mathbf{F}_{n+1} - \mathbf{F}_n)), \quad (56)$$

then

$$w'(t) = \frac{\partial \Psi}{\partial \mathbf{F}}(\mathbf{F}_n + t(\mathbf{F}_{n+1} - \mathbf{F}_n)) : (\mathbf{F}_{n+1} - \mathbf{F}_n). \quad (57)$$

Due to the convexity assumption of $\Psi(\mathbf{F})$, we have

$$w'(1) \geq w(1) - w(0). \quad (58)$$

This gives:

$$\frac{\partial \Psi}{\partial \mathbf{F}}(\mathbf{F}_{n+1}) : (\mathbf{F}_{n+1} - \mathbf{F}_n) \geq \Psi(\mathbf{F}_{n+1}) - \Psi(\mathbf{F}_n). \quad (59)$$

Using (35) we have

$$\delta t \frac{\partial \Psi}{\partial \mathbf{F}}(\mathbf{F}_{n+1}) : \nabla_{\hat{\mathbf{x}}} \mathbf{u}_{n+1} \geq \Psi(\mathbf{F}_{n+1}) - \Psi(\mathbf{F}_n). \quad (60)$$

which finally leads to (55) by integrating (60) in $\Omega_{t_0}^s$. \square

Due to the arbitrariness of \mathbf{v} , q and \mathbf{z} , we now choose $\mathbf{v} = \mathbf{u}_{n+1}^h$, $q = -p_{n+1}^h$ and $\mathbf{z} = 0$ in equation (42) to deduce the stability result. Using Lemma 1, we have

$$\begin{aligned} & \rho \int_{\Omega_{t_{n+1}}} \mathbf{u}_{n+1}^h \cdot \mathbf{u}_{n+1}^h - \rho \int_{\Omega_{t_n}} \mathbf{u}_n^h \cdot \mathbf{u}_{n+1}^h \\ & + \delta t \rho \mathcal{I}(\xi(t)) + \frac{\delta t \mu^f}{2} \int_{\Omega_{t_{n+1}}^f} \mathbf{D} \mathbf{u}_{n+1}^h : \mathbf{D} \mathbf{u}_{n+1}^h \\ & + \delta t \int_{\Omega_{t_0}^s} \frac{\partial \Psi}{\partial \mathbf{F}}(\mathbf{F}_{n+1}) : \nabla_{\hat{\mathbf{x}}} \mathbf{u}_{n+1}^h = \delta t \int_{\Omega_{t_{n+1}}} \rho \mathbf{g} \cdot \mathbf{u}_{n+1}^h. \end{aligned} \quad (61)$$

Combining Lemmas 2 and 3 we have

$$\|\mathbf{u}_{n+1}\|_{0, \Omega_{t_n}}^2 = \|\mathbf{u}_{n+1}\|_{0, \Omega_{t_{n+1}}}^2 - \delta t \mathcal{I}(\eta) = \|\mathbf{u}_{n+1}\|_{0, \Omega_{t_{n+1}}}^2 + \delta t \mathcal{I}(\xi). \quad (62)$$

Substituting equation (62) into the following estimate

$$\begin{aligned} & \int_{\Omega_{t_n}} \mathbf{u}_n^h \cdot \mathbf{u}_{n+1}^h \leq \|\mathbf{u}_n^h\|_{0, \Omega_{t_n}} \|\mathbf{u}_{n+1}^h\|_{0, \Omega_{t_n}} \\ & \leq \frac{1}{2} \left(\|\mathbf{u}_n^h\|_{0, \Omega_{t_n}}^2 + \|\mathbf{u}_{n+1}^h\|_{0, \Omega_{t_n}}^2 \right), \end{aligned} \quad (63)$$

we get

$$\int_{\Omega_{t_n}} \mathbf{u}_n^h \cdot \mathbf{u}_{n+1}^h \leq \frac{1}{2} \left(\|\mathbf{u}_n^h\|_{0, \Omega_{t_n}}^2 + \|\mathbf{u}_{n+1}^h\|_{0, \Omega_{t_{n+1}}}^2 + \delta t \mathcal{I}(\xi) \right). \quad (64)$$

Combining (61) and (64), and thanks to Lemma 4 the energy stability result reads:

105

Proposition 1 (Energy non-increasing). *Let $(\mathbf{u}_{n+1}^h, p_{n+1}^h, \mathbf{w}_{n+1}^h)$ be the solution of Problem 2, if there is no body force, then*

$$\begin{aligned} & \frac{\rho}{2} \|\mathbf{u}_{n+1}^h\|_{0, \Omega_{t_{n+1}}}^2 + E(t_{n+1}) + \frac{\delta t \mu^f}{2} \sum_{k=1}^{n+1} \int_{\Omega_{t_k}^f} \mathbf{D}\mathbf{u}_k^h : \mathbf{D}\mathbf{u}_k^h d\mathbf{x} \\ & \leq \frac{\rho}{2} \|\mathbf{u}_n^h\|_{0, \Omega_{t_n}}^2 + E(t_n) + \frac{\delta t \mu^f}{2} \sum_{k=1}^n \int_{\Omega_{t_k}^f} \mathbf{D}\mathbf{u}_k^h : \mathbf{D}\mathbf{u}_k^h d\mathbf{x}. \end{aligned} \quad (65)$$

The above estimate indicate that the total energy, including kinetic energy, potential energy and the viscous dissipation, of the FSI system is non-increasing.

Remark 4. *The stability result (Proposition 1) is drawn under assumption of the homogeneous Dirichlet and Neumann boundary conditions (17), and without any body force. In this enclosed system, we prove that the interactions between fluids and solid in the FSI system is stable. Although the stability is only proved using an enclosed system, this also provides a strong indication of stability for other FSI systems if the input energy is stable.*

6. Implementation: F-scheme and d-scheme

In this section, we focus on the implementation of a specific solid model, which determines the following term

$$\int_{\Omega_{t_0}^s} \frac{\partial \Psi}{\partial \mathbf{F}}(\mathbf{F}_{n+1}) : \nabla_{\hat{\mathbf{x}}} \mathbf{v} \quad (66)$$

in equation (42). We consider an incompressible neo-Hookean solid model with the energy function Ψ being given as follows [30]:

$$\Psi(\mathbf{F}) = \frac{c_1}{2} [\text{tr}(\mathbf{F}\mathbf{F}^T) - d - 2\ln(J_{\mathcal{F}_t})]. \quad (67)$$

In order to compute the derivative of Ψ with respect to \mathbf{F} , we first have

$$\begin{aligned} \left[\frac{\partial \text{tr}(\mathbf{F}^T \mathbf{F})}{\partial \mathbf{F}} \right]_{mn} &= \frac{\partial \text{tr}(F_{ki} F_{kj})}{\partial F_{mn}} = \frac{\partial \sum_k^d \sum_i^d F_{ki}^2}{\partial F_{mn}} \\ &= \frac{\partial (F_{11}^2 + F_{12}^2 + \dots + F_{dd}^2)}{\partial F_{mn}} = 2\mathbf{F}_{mn}. \end{aligned} \quad (68)$$

Let $\text{cof}(F_{ij}) = (-1)^{i+1} \det(\mathbf{F} \text{ without } i^{\text{th}} \text{ row and } j^{\text{th}} \text{ column})$ be the cofactor of F_{ij} . Because of $J_{\mathcal{F}_t} = \sum_k^d F_{ik} \text{cof}(F_{ik})$, we have $\frac{\partial J_{\mathcal{F}_t}}{\partial F_{ij}} = \text{cof}(F_{ij})$, i.e.,

$$\frac{\partial J_{\mathcal{F}_t}}{\partial \mathbf{F}} = \text{cof}(\mathbf{F}) = J_{\mathcal{F}_t} \mathbf{F}^{-T}. \quad (69)$$

Combining equations (68) and (69) gives

$$\frac{\partial \Psi}{\partial \mathbf{F}} = c_1 (\mathbf{F} - \mathbf{F}^{-T}). \quad (70)$$

Using formula (35), the term (66) can then be expressed as:

$$\begin{aligned}
& \int_{\Omega_{t_0}^s} \frac{\partial \Psi}{\partial \mathbf{F}} (\mathbf{F}_{n+1}) : \nabla_{\hat{\mathbf{x}}} \mathbf{v} = c_1 \int_{\Omega_{t_0}^s} (\mathbf{F}_{n+1} - \mathbf{F}_{n+1}^{-T}) : \nabla_{\hat{\mathbf{x}}} \mathbf{v} \\
& = c_1 \int_{\Omega_{t_0}^s} \mathbf{F}_{n+1} : \nabla_{\hat{\mathbf{x}}} \mathbf{v} - c_1 \int_{\Omega_{t_{n+1}}^s} J_{\mathcal{F}_t}^{-1} \nabla \cdot \mathbf{v} \\
& = c_1 \delta t \int_{\Omega_{t_0}^s} \nabla_{\hat{\mathbf{x}}} \mathbf{u}_{n+1} : \nabla_{\hat{\mathbf{x}}} \mathbf{v} + c_1 \int_{\Omega_{t_0}^s} \mathbf{F}_n : \nabla_{\hat{\mathbf{x}}} \mathbf{v} - c_1 \int_{\Omega_{t_{n+1}}^s} J_{\mathcal{F}_t}^{-1} \nabla \cdot \mathbf{v}.
\end{aligned} \tag{71}$$

In the above we update the solid deformation tensor \mathbf{F} and integrate in the initial configuration, and we call this the \mathbf{F} -scheme. We can also express the stress in terms of displacement \mathbf{d} and integrate in the current configuration as introduced in [6], which is called the \mathbf{d} -scheme. To deduce the \mathbf{d} -scheme, we first transform the term (66) to be integrated in the current domain:

$$\int_{\Omega_{t_0}^s} \frac{\partial \Psi}{\partial \mathbf{F}} (\mathbf{F}_{n+1}) : \nabla_{\hat{\mathbf{x}}} \mathbf{v} = \int_{\Omega_{t_{n+1}}^s} J_{\mathcal{F}_t}^{-1} \frac{\partial \Psi}{\partial \mathbf{F}} \mathbf{F}^T : \nabla \mathbf{v} = \int_{\Omega_{t_{n+1}}^s} \boldsymbol{\tau}^s : \nabla \mathbf{v}, \tag{72}$$

where

$$\boldsymbol{\tau}^s = c_1 J_{\mathcal{F}_t}^{-1} (\mathbf{B} - \mathbf{I}) \tag{73}$$

is the deviatoric stress tensor, with $\mathbf{B} = \mathbf{F}\mathbf{F}^T$.

Let us only consider a two dimensional case, readers may refer to [21] for the three dimensional case. According to the Cayley-Hamilton theorem, \mathbf{B} satisfies its characteristic equation:

$$\mathbf{B}^2 - tr_{\mathbf{B}} \mathbf{B} + J_{\mathcal{F}_t}^2 \mathbf{I} = 0, \tag{74}$$

from which we immediately have:

$$\mathbf{B} = tr_{\mathbf{B}} \mathbf{I} - J_{\mathcal{F}_t}^2 \mathbf{B}^{-1}. \tag{75}$$

Since

$$\mathbf{F} = \nabla_{\hat{\mathbf{x}}} \mathbf{x} = \nabla_{\hat{\mathbf{x}}} (\hat{\mathbf{x}} + \mathbf{d}) = \mathbf{I} + \mathbf{F} \nabla \mathbf{d}, \tag{76}$$

we also have:

$$\mathbf{F}^{-1} = \mathbf{I} - \nabla \mathbf{d}. \tag{77}$$

Substituting (75) and (77) into (73), $\boldsymbol{\tau}^s$ can be expressed by displacement as follows:

$$\boldsymbol{\tau}^s = -c_1 J_{\mathcal{F}_t} (\mathbf{I} - \nabla \mathbf{d})^T (\mathbf{I} - \nabla \mathbf{d}) + c_1 J_{\mathcal{F}_t}^{-1} (tr_{\mathbf{B}} - 1) \mathbf{I}, \tag{78}$$

which can further be written as

$$\boldsymbol{\tau}^s = c_1 J_{\mathcal{F}_t} (\mathbf{D} \mathbf{d} - \nabla^T \mathbf{d} \nabla \mathbf{d}) + \bar{p} \mathbf{I}, \tag{79}$$

where $\bar{p} = c_1 J_{\mathcal{F}_t}^{-1} (\text{tr} \mathbf{B} - 1) - c_1 J_{\mathcal{F}_t}$ will be integrated into the solid pressure p in (11) as an unknown. Similarly to the update of \mathbf{F} in (35), updating the displacement by

$$\mathbf{d}_{n+1} = \tilde{\mathbf{d}}_n + \delta t \mathbf{u}_{n+1}, \quad \tilde{\mathbf{d}}_n = \mathbf{d}_n \circ \mathcal{A}_{t_n, t_{n+1}}^{-1}, \quad (80)$$

leads to the computation of term (66) as follows:

$$\begin{aligned} & \int_{\Omega_{i_0}^s} \frac{\partial \Psi}{\partial \mathbf{F}} (\mathbf{F}_{n+1}) : \nabla_{\tilde{\mathbf{x}}} \mathbf{v} = \int_{\Omega_{i_{n+1}}^s} \boldsymbol{\tau}^s : \nabla \mathbf{v} \\ & = c_1 \int_{\Omega_{i_{n+1}}^s} (\mathbf{D} \mathbf{d}_{n+1} - \nabla^T \mathbf{d}_{n+1} \nabla \mathbf{d}_{n+1}) : \nabla \mathbf{v} \\ & = \frac{c_1 \delta t}{2} \int_{\Omega_{i_{n+1}}^s} \mathbf{D} \mathbf{u}_{n+1} : \mathbf{D} \mathbf{v} + \frac{c_1}{2} \int_{\Omega_{i_{n+1}}^s} \mathbf{D} \tilde{\mathbf{d}}_n : \mathbf{D} \mathbf{v} \\ & \quad - \delta t c_1 \int_{\Omega_{i_{n+1}}^s} \left(\nabla^T \mathbf{u}_{n+1} \nabla \tilde{\mathbf{d}}_n + \nabla^T \tilde{\mathbf{d}}_n \nabla \mathbf{u}_{n+1} \right) : \nabla \mathbf{v} \\ & \quad - c_1 \int_{\Omega_{i_{n+1}}^s} \nabla^T \tilde{\mathbf{d}}_n \nabla \tilde{\mathbf{d}}_n : \nabla \mathbf{v}. \end{aligned} \quad (81)$$

Note that in the above, the second order term $O(\delta t^2)$ is neglected and $J_{\mathcal{F}_t}$ is replaced by 1. The stability of the \mathbf{d} -scheme is proved in [6] with the neglect of the term of order $O(\delta t^2)$, which may be regarded as a further approximation of the \mathbf{F} -scheme.

Remark 5. *The two and three dimensional \mathbf{F} -scheme have exactly the same formulations. This can be seen from equation (71), which does not depend on dimensions. However the formulation of the \mathbf{d} -scheme depends on the Cayley-Hamilton theorem, which is different in two and three dimensions, and consequently leads to significant complexity of the \mathbf{d} -scheme in three dimensions [21]. It should be noted however that an advantage of the \mathbf{d} -scheme is that, because it computes all integrals in the current domain, it is more straight forward to handle remeshing when it is required [6].*

Remark 6. *Notice that equation (80) is a backward-Euler approximation for displacement \mathbf{d} rather than velocity \mathbf{u} . This choice is consistent with the overall first-order time discretisation. The mid-point rule is another choice, however the overall scheme is still first order, because the update of domain Ω_t is not straightforward to compute to second order [6, 31].*

7. Numerical experiments

In this section, we assess the reliability and stability of the proposed numerical scheme through a selection of benchmarks in the FSI area. We shall use the Taylor-Hood elements for the velocity-pressure pair. We validate the energy

841
842
843
844
845
846
847
848
849
850
140
851
852
853
854
855
145
856
857

stability expressed by (65) in Section 7.1. We validate the proposed scheme against a FSI problem with a semi-analytic solution in Section 7.2. Time and mesh convergence tests are carried out in Section 7.3, and an example with very large solid deformation is tested in Section 7.4. The **F**-scheme will be adopted in all the following numerical tests. In addition, the **d**-scheme is also implemented for tests in Section 7.1 and 7.4 in order to compare the two schemes.

We use the following consistent units for all the numerical tests in this section: length (m), time (s), velocity (m/s), acceleration (m/s^2), mass (kg), force (N), pressure/stress (N/m^2), density (kg/m^3) and viscosity ($N \cdot s/m^2$).

7.1. Oscillating disc

858
859
860
861
862
863

In this test, we consider an enclosed flow ($\mathbf{n} \cdot \mathbf{u} = 0$) in $\Omega = [0, 1] \times [0, 1]$ with a periodic boundary condition. A solid disc is initially located in the middle of the square Ω and has a radius of 0.2. The initial velocity of the fluid and solid are prescribed by the following stream function

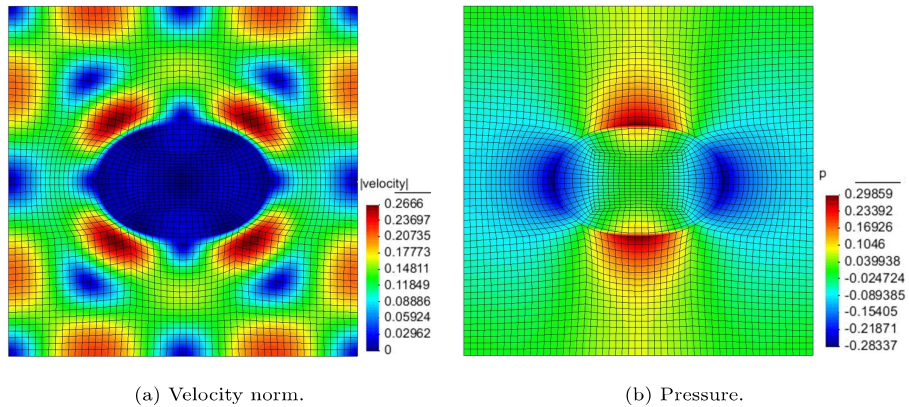
$$\Psi = \Psi_0 \sin(ax) \sin(by),$$

864
865
866
867
868
869
870
871
150
872
873
874
875
876
877
878
879
880
881
882
883
884
885
886

where $\Psi_0 = 5.0 \times 10^{-2}$ and $a = b = 2\pi$. In this test, $\rho^f = 1$, $\mu^f = 0.01$, $\rho^s = 1.5$ and $c_1 = 1$. Taking the maximum initial velocity $2\pi\Psi_0 = \hat{U}$ and the height of domain Ω , $\hat{H} = 1$, as the characteristic velocity and length respectively, the Reynolds number is: $Re = \frac{\rho^f \hat{U} \hat{H}}{\mu^f} = 10\pi$. A mesh size of 3217 elements with 13081 nodes is used in this test. In order to visualize the flow a snapshot ($t = 0.25$) of the velocity and pressure field are presented in Figure 2, and the evolution of energy is presented in Figure 3 and 4 from which we can observe the property of non-increasing total energy as proved in Proposition 1.

155
872
873
874
875
876
877
878
879
880
881
882
883
884
885
886

The **F**-scheme and **d**-scheme are compared using this example and we have not found any significant difference by comparing the solid deformation as shown in Figure 5.



887
888
889
890
891
892
893
894
895
896

Figure 2: Snapshot of the oscillating disc at $t = 0.25$ when the disc is maximally stretched, using a time step of $\Delta t = 0.01$.

897
 898
 899
 900
 901
 902
 903
 904
 905
 906
 907
 908
 909
 910
 911
 912
 913
 914
 915
 916
 917
 918
 919
 920
 921
 922
 923
 924
 925
 926
 927
 928
 929
 930
 931
 932
 933
 934
 935
 936
 937
 938
 939
 940
 941
 942
 943
 944
 945
 946
 947
 948
 949
 950
 951
 952

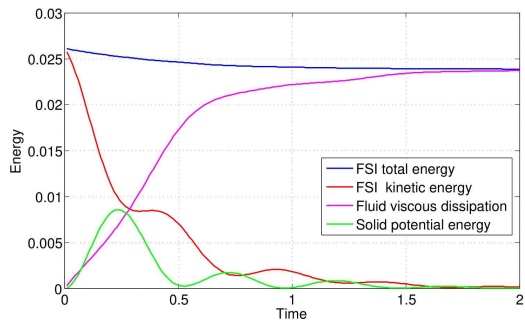


Figure 3: Evolution of energy for the oscillating disc using $\Delta t = 0.01$. The peaks of the green curve indicate the time when the disc is maximally stretched. The first peak is horizontally stretched and the second peak is vertically stretched. The troughs of the green curve are the stress-free stages.

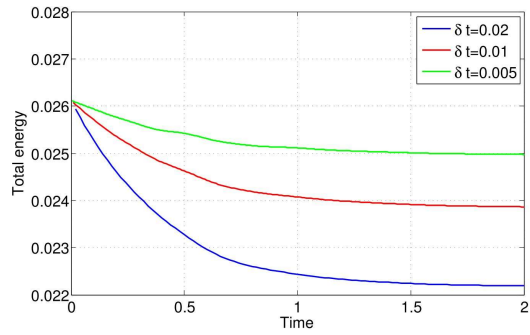


Figure 4: Evolution of total energy for the oscillating disc.

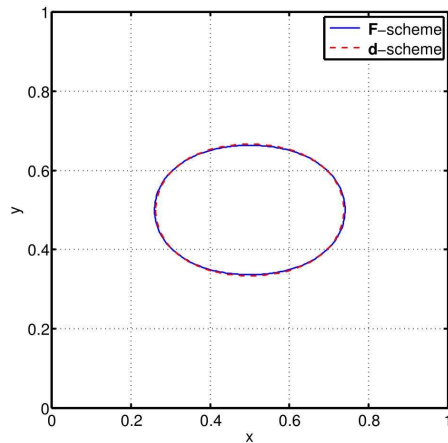


Figure 5: Comparison of disc shape for the **F**-scheme and **d**-scheme at $t = 0.25$ when the disc is maximally stretched.

953
954
955
956
957
958
959
960
961
962
963
964
965
966
967
968
969
970
971
972
973
974
975
976
977
978
979
980
981
982
983
984
985
986
987
988
989
990
991
992
993
994
995
996
997
998
999
1000
1001
1002
1003
1004
1005
1006
1007
1008

7.2. Rotating disc

This test is taken from [6]. The computational domain is the area between two concentric circles (R_0 and R_1) as shown in Figure 6, with fluid and solid properties as $\rho^f = 1, \rho^s = 2, \mu^f = 2$ and $c_1 = 4$. A constant angular velocity ($\omega = U/R_1 = 0.6$) is prescribed at the outer boundary and the velocity on the inner boundary is set to be zero. Taking the value of velocity U and length R_1 as references, the Reynolds number is: $Re = \frac{\rho^f U R_1}{\mu^f} = 7.5$. This velocity first induces the fluid, that is initially at rest, to rotate and then gradually drags the solid to rotate as well. For a long-term run, the solid disc will oscillate, and its velocity will finally be damped to 0 as shown in Figure 7. However, in this paper we are interested in time $t=0.85$ when the solid has its largest deformation. Using the property of symmetry, this problem can be reduced to a one-dimensional equation when considered in a polar coordinate system (r, θ) [6]:

$$\rho^f \frac{\partial u_\theta}{\partial t} = \frac{\mu^f}{r} \frac{\partial}{\partial r} \left(r \frac{\partial u_\theta}{\partial r} \right) - \mu^f \frac{u_\theta}{r^2}, \quad R \leq r < R_1 \quad (82)$$

and

$$\rho^s \frac{\partial u_\theta}{\partial t} = \frac{c_1}{r} \frac{\partial}{\partial r} \left(r \frac{\partial d_\theta}{\partial r} \right) - c_1 \frac{d_\theta}{r^2}, \quad \frac{\partial d_\theta}{\partial t} = u_\theta, \quad R_0 < r \leq R, \quad (83)$$

where u_r and u_θ are the velocity components in the radial and tangential directions respectively. This one-dimensional problem (82) and (83) can be solved numerically to high accuracy, and the solution is plotted in Figure 7 using 200 linear elements and $\Delta t = 1.0 \times 10^{-3}$. Using the same time step, which is stable, the proposed method can produce results of similar accuracy to the semi-analytic solution (i.e. the high-accuracy numerical solution of (82) and (83)), as shown in Figure 8. We use three different meshes to test convergence of the proposed algorithm. A coarse mesh equally divides the radial direction of the computational domain into 4 segments, and equally divides the tangential direction into to 40 segments, which therefore has $4 \times 40 = 160$ biquadratic elements. The medium and fine meshes are refined based on the coarse mesh, which have $8 \times 80 = 640$ and $16 \times 160 = 2560$ elements respectively. Due to the discontinuity in the derivative at the fluid-solid interface, we only achieve an $O(h)$ convergence as shown in Figure 9, where h is the mesh size. This observation is consistent with the result in [6].

7.3. Oscillating flag

In this section, we consider an oscillating flag attached to a cylinder, which was firstly proposed in [32] (named FSI3), and been regarded as a challenging numerical test in the FSI field. We test the time and mesh convergence for the proposed FSI method. The computational domain is a rectangle ($L \times H$) with a cut hole of radius r and center (c, c) as shown in Figure 10. A leaflet of size $l \times h$ is attached to the boundary of the hole (the mesh of the leaflet is fitted to the boundary of the hole, see the solid mesh in Figure 11). In this test,

1009
 1010
 1011
 1012
 1013
 1014
 1015
 1016
 1017
 1018
 1019
 1020
 1021
 1022
 1023
 1024
 1025
 1026
 1027
 1028
 1029
 1030
 1031
 1032
 1033
 1034
 1035
 1036
 1037
 1038
 1039
 1040
 1041
 1042
 1043
 1044
 1045
 1046
 1047
 1048
 1049
 1050
 1051
 1052
 1053
 1054
 1055
 1056
 1057
 1058
 1059
 1060
 1061
 1062
 1063
 1064

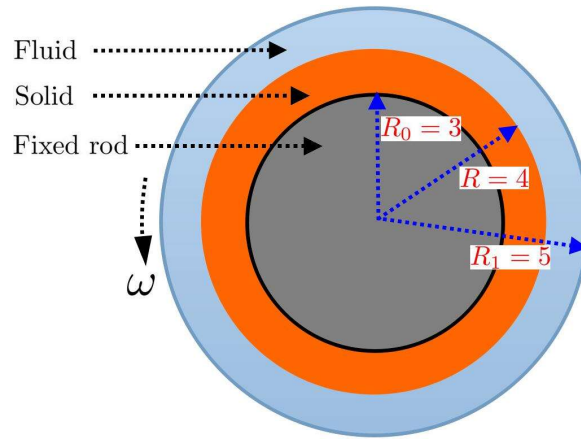


Figure 6: Sketch of a rotating disc in Section 7.2.

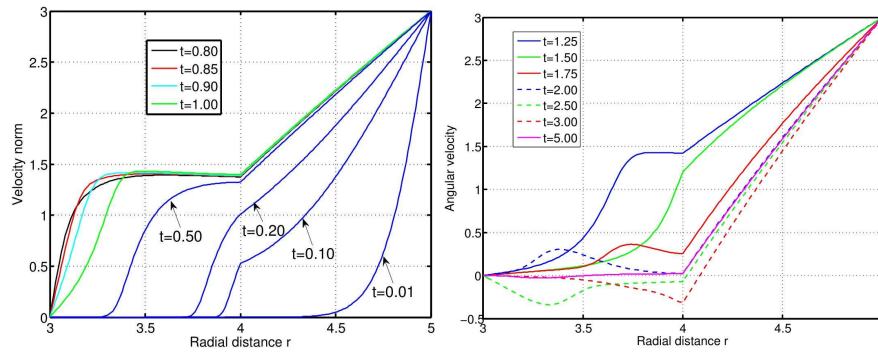


Figure 7: Evolution of the velocity norm for the reduced one-dimensional rotating disc.

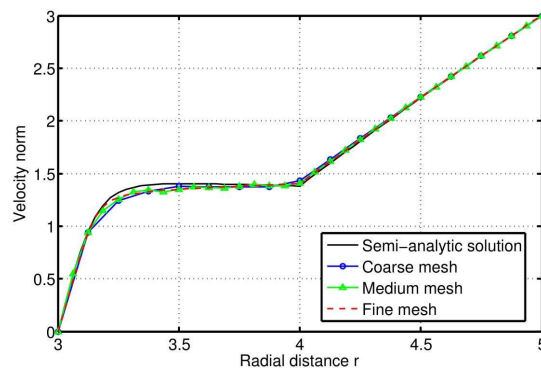


Figure 8: Comparison between the proposed approach and the semi-analytic solution at $t = 0.85$ when the solid is maximally deformed.

1065
1066
1067
1068
1069
1070
1071
1072
1073
1074
1075
1076
1077
1078
1079
1080
1081
1082
1083
1084
1085
1086
1087
1088
1089
1090
1091
1092
1093
1094
1095
1096
1097
1098
1099
1100
1101
1102
1103
1104
1105
1106
1107
1108
1109
1110
1111
1112
1113
1114
1115
1116
1117
1118
1119
1120

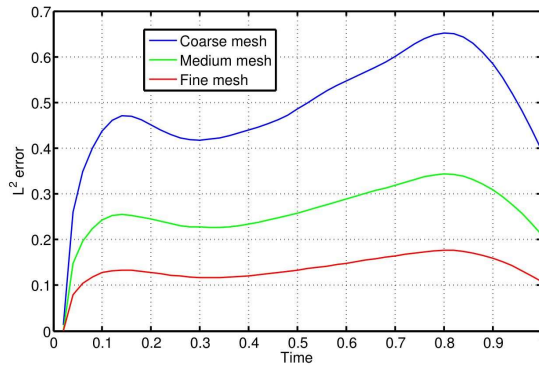


Figure 9: Convergence of L^2 error.

$L = 2.5$, $H = 0.41$, $l = 0.35$, $h = 0.02$, $c = 0.2$ and $r = 0.05$. The fluid and solid parameters are as follows: $\rho^f = \rho^s = 10^3$, $\mu^f = 1$ and $c_1 = 2.0 \times 10^6$. Taking $\bar{U} = \int_0^H \bar{u}_x dy = 2H$ and the channel height H as the characteristic velocity and length respectively, the Reynolds number is: $Re = \frac{\rho^f \bar{U} H}{\mu^f} = 336.2$. The inlet flow is prescribed as:

$$\bar{u}_x = \frac{12y}{H^2} (H - y), \quad \bar{u}_y = 0. \quad (84)$$

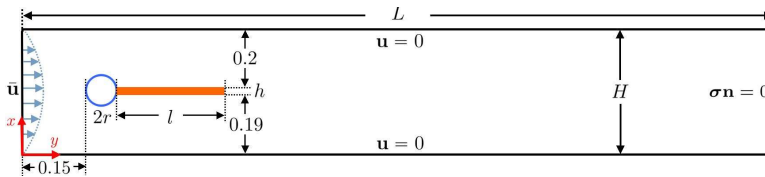


Figure 10: Computational domain and boundary conditions for the oscillating flag.

175 A wall boundary condition and the outlet flow condition are displayed in Figure 10. A coarse mesh has 10054 nodes and 2448 biquadratic elements as shown in Figure 11, and a medium and fine mesh have 33746 nodes (8320 elements) and 68974 nodes (17081 elements) respectively. We study the oscillating frequency and amplitude at the tip of the flag. The convergence with respect to time and space are displayed in Figure 12 and Figure 13 respectively, and the period and amplitude of the oscillation converge to 5.26×10^{-3} and 0.0018 ± 0.0365 respectively. 180
1106 and amplitude of the oscillation converge to 5.26×10^{-3} and 0.0018 ± 0.0365 respectively. These figures have a good agreement with the reference values given in [32] with oscillation period and amplitude being 5.3×10^{-3} and 0.00148 ± 0.03438 respectively.

185 7.4. Falling disc

In this test, we simulate a falling disc due to gravity [30, 33], which needs remeshing in order to guarantee the mesh quality. However we will demonstrate

1121
1122
1123
1124
1125
1126
1127
1128
1129
1130
1131
1132
1133
1134
1135
1136
1137
1138
1139
1140
1141
1142
1143
1144
1145
1146
1147
1148
1149
1150
1151
1152
1153
1154
1155
1156
1157
1158
1159
1160
1161
1162
1163
1164
1165
1166
1167
1168
1169
1170
1171
1172
1173
1174
1175
1176

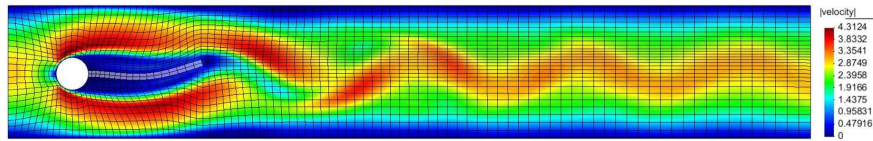


Figure 11: A snap shot of the velocity norms at $t=6$ using a coarse mesh.

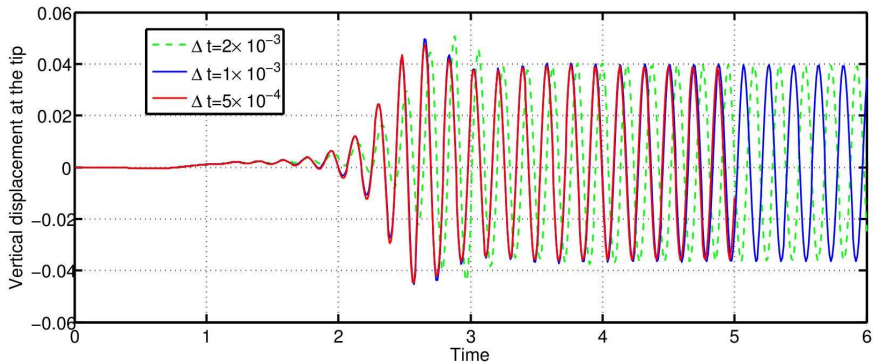


Figure 12: Vertical displacement at the flag tip as a function of time, using different time step and a medium mesh (data of the red curve is plotted up to $t = 5$ for a better visualisation of the blue curve).

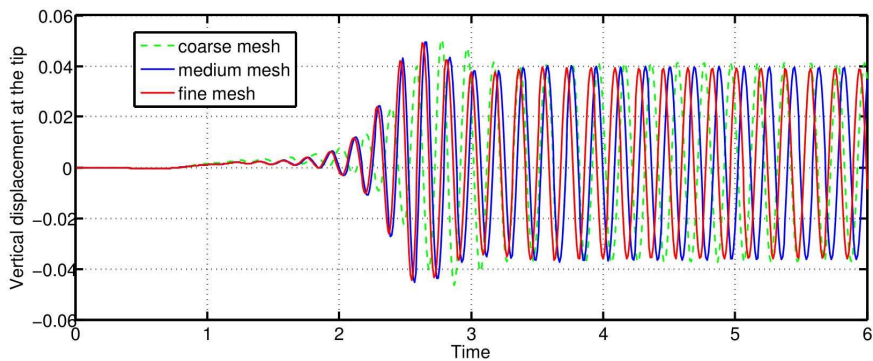


Figure 13: Vertical displacement at the flag tip as a function of time, using different mesh size and a time step size of $\Delta t = 5 \times 10^{-4}$.

that one needs much less remeshing, using the proposed ALE methods, compared to methods using pure remesh in order to fit the fluid-solid interface [6].
190 This test is implemented using FreeFEM++ [34].

The computational domain is a vertical channel with a disc placed at the top of the channel as illustrated in Figure 14, where $W = 4$, $H = 12$, $h = 2$ and $R = 1$. In this test, $\rho^f = 1$, $\rho^s = 1.5$, $\mu^f = 0.1$, $c_1 = 10^4$ and the gravity acceleration is $g = -9.81$. The fluid velocity is fixed to be 0 on all boundaries except the top, which uses the zero-normal-stress boundary condition, i.e. $\boldsymbol{\sigma} \mathbf{n} = \mathbf{0}$. Notice that we choose c_1 sufficiently large so that the solid behaves as a rigid

1177
1178
1179
1180
1181
1182
1183
1184
1185
1186
1187
1188
1189
1190
1191
1192
1193
1194
1195
1196
1197
1198
1199
1200
1201
1202
1203
1204
1205
1206
1207
1208
1209
1210
1211
1212
1213
1214
1215
1216
1217
1218
1219
1220
1221
1222
1223
1224
1225
1226
1227
1228
1229
1230
1231
1232

body. The computational domain is initially discretised by using 820 P_2/P_1 triangles with 1713 nodes as shown in Figure 15. We use a stable time step size of $\delta t = 0.01$ and remesh every 100 times. We compare the simulation result against the empirical solution of a rigid ball falling in a viscous fluid [35], for which the maximal velocity U_m under gravity is given by

$$U_m = \frac{(\rho^s - \rho^f) g R^2}{4\mu^f} \left[\ln \left(\frac{W}{2R} \right) - 0.9157 + 1.7244 \left(\frac{2R}{W} \right)^2 - 1.7302 \left(\frac{2R}{W} \right)^4 \right].$$

In the test $U_m = 1.2263$. Taking this final velocity U_m and the disc radius R as the characteristic velocity and length respectively, the Reynolds number is: $Re = \frac{\rho^f U_m R}{\mu^f} = 12.263$. The numerical and the empirical solutions agree well with each other when disc becomes stable as shown in Figure 16. It can be understood that the disc velocity gradually decreases when it is close to the bottom of the channel. The evolution of the disc is displayed in Figure 17. If we move the mesh by fluid velocity without the proposed ALE techniques, and remesh to guarantee the mesh quality then, for this example, we find that remeshing has to be taken at least every 7 time steps, otherwise the disc cannot successfully arrive at the bottom of the channel. We have also compared the **F**-scheme and **d**-scheme using this numerical test, and found that they presented very similar results (hence the latter are not shown in the figures here).

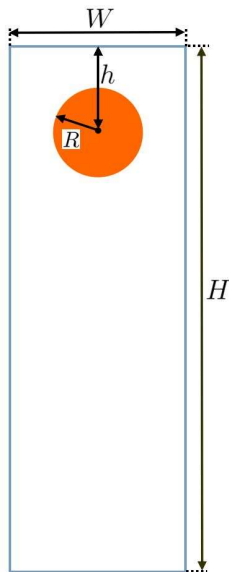


Figure 14: Sketch of the falling disc.

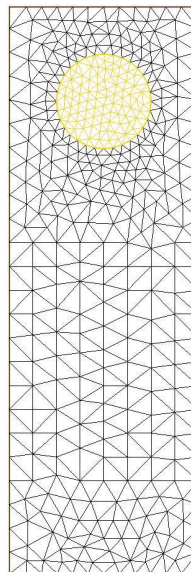


Figure 15: Initial mesh for the falling disc.

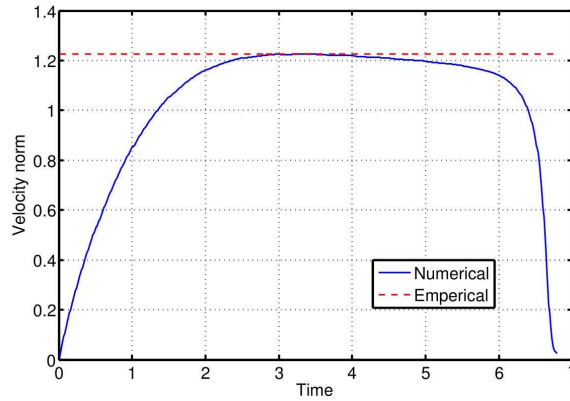


Figure 16: Comparison between the numerical and empirical velocity of the falling disc.

8. Conclusion

In this paper, we develop the one-field finite element method for Fluid-Structure Interaction (FSI), which only solves one-velocity field in the whole domain. We formulate the FSI system in an Arbitrary Lagrangian-Eulerian (ALE) coordinate system, solve it in a fully-coupled manner, and prove this ALE-FSI formulation is unconditionally stable by analysing the total energy of the whole system. The stability result is achieved by expressing the problem in a conservative form, and adopting an exact quadrature rule in order to eliminate the mesh velocity. Several numerical tests are presented in order to validate the proposed scheme, including testing the energy stability, validating against a semi-analytical solution and a benchmark case, and combining with a remeshing technique to simulate the case of extremely large solid displacement.

The stability proofs given in this manuscript are restricted to the case where the backward Euler scheme is applied in time. We expect the forward Euler scheme to be conditionally stable but potentially with much more restrictive time-step size than in the implicit case. We have not analysed the use of other implicit time-discretisation schemes, such as BDF2 or Crank-Nicolson, since these add significant complexity to the problem. In particular, as with all ALE schemes, the stability depends critically on the unknown mesh velocities, which makes the analysis very challenging in these higher order cases.

We test a variety of numerical examples, including a strong non-linear FSI problem such as the oscillating flag in test 7.3, which is regarded as a challenging benchmark in the FSI field. In none of the test cases that we have considered have we observed any instabilities.

References

- [1] K. H. Bendiksen, D. Maines, R. Moe, S. Nuland, et al., The dynamic two-fluid model OLGA: Theory and application, SPE Production Engineering 6 (02) (1991) 171–180.

1289
 1290
 1291
 1292
 1293
 1294
 1295
 1296
 1297
 1298
 1299
 1300
 1301
 1302
 1303
 1304
 1305
 1306
 1307
 1308
 1309
 1310
 1311
 1312
 1313
 1314
 1315
 1316
 1317
 1318
 1319
 1320
 1321
 1322
 1323
 1324
 1325
 1326
 1327
 1328
 1329
 1330
 1331
 1332
 1333
 1334
 1335
 1336
 1337
 1338
 1339
 1340
 1341
 1342
 1343
 1344

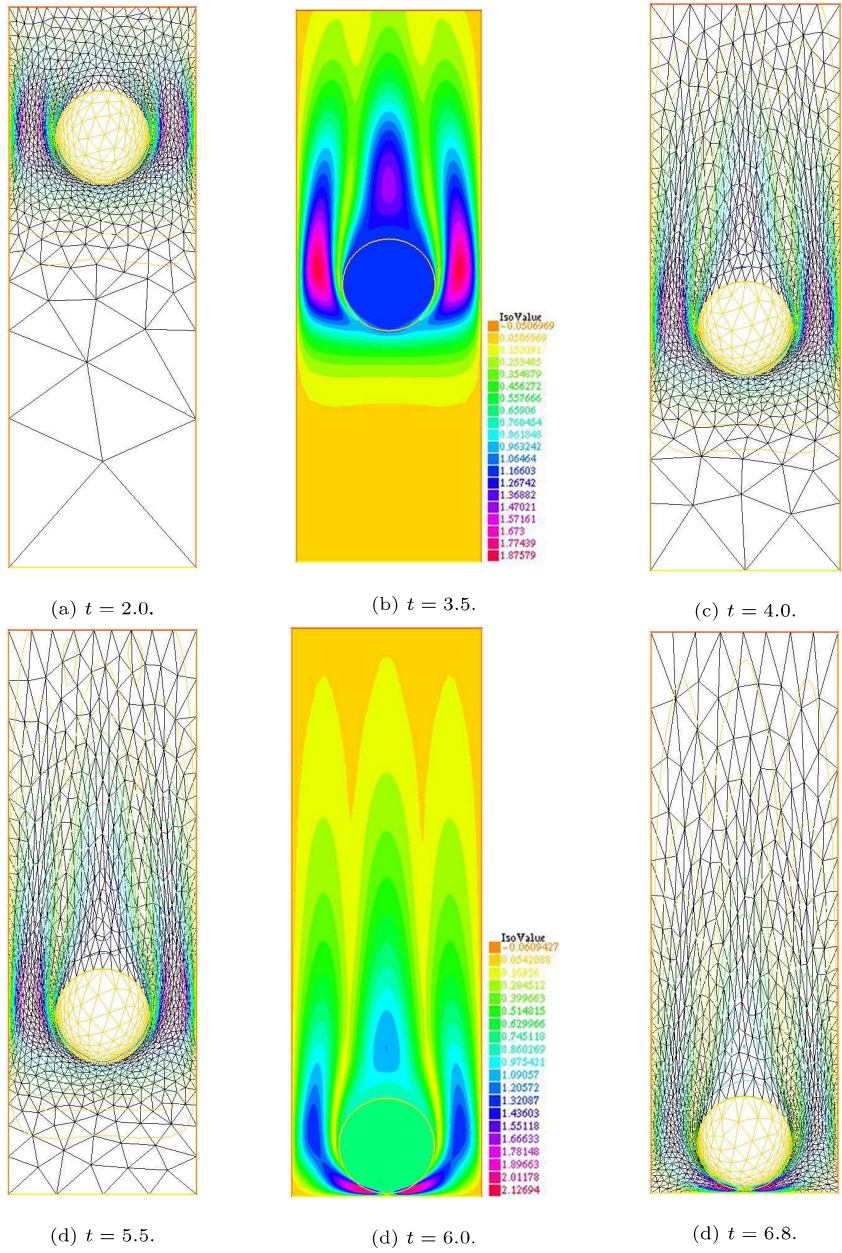


Figure 17: Evolution of the falling disc, with colour showing the velocity norm.

[2] F. J. Blom, A monolithic fluid-structure interaction algorithm applied to the piston problem, *Computer Methods in Applied Mechanics and Engineering* 167 (3-4) (1998) 369–391.

- 1345
1346
1347
1348
1349
1350
1351
1352
1353
1354
1355
1356
1357
1358
1359
1360
1361
1362
1363
1364
1365
1366
1367
1368
1369
1370
1371
1372
1373
1374
1375
1376
1377
1378
1379
1380
1381
1382
1383
1384
1385
1386
1387
1388
1389
1390
1391
1392
1393
1394
1395
1396
1397
1398
1399
1400
- [3] M. Heil, An efficient solver for the fully coupled solution of large-displacement fluid–structure interaction problems, *Computer Methods in Applied Mechanics and Engineering* 193 (1-2) (2004) 1–23. doi:10.1016/j.cma.2003.09.006.
- [4] M. Heil, A. L. Hazel, J. Boyle, Solvers for large-displacement fluid–structure interaction problems: segregated versus monolithic approaches, *Computational Mechanics* 43 (1) (2008) 91–101. doi:10.1007/s00466-008-0270-6.
- [5] R. L. Muddle, M. Mihajlović, M. Heil, An efficient preconditioner for monolithically-coupled large-displacement fluid–structure interaction problems with pseudo-solid mesh updates, *Journal of Computational Physics* 231 (21) (2012) 7315–7334. doi:10.1016/j.jcp.2012.07.001.
- [6] F. Hecht, O. Pironneau, An energy stable monolithic Eulerian fluid–structure finite element method, *International Journal for Numerical Methods in Fluids* 85 (7) (2017) 430–446. doi:10.1002/flid.4388.
- [7] Y. Wang, P. K. Jimack, M. A. Walkley, A one-field monolithic fictitious domain method for fluid–structure interactions, *Computer Methods in Applied Mechanics and Engineering* 317 (2017) 1146–1168. doi:10.1016/j.cma.2017.01.023.
- [8] Y. Wang, P. K. Jimack, M. A. Walkley, Energy analysis for the one-field fictitious domain method for fluid-structure interactions, *Applied Numerical Mathematics* 140 (2019) 165–182. doi:10.1016/j.apnum.2019.02.003.
- [9] B. Hübner, E. Walhorn, D. Dinkler, A monolithic approach to fluid–structure interaction using space–time finite elements, *Computer Methods in Applied Mechanics and Engineering* 193 (23-26) (2004) 2087–2104.
- [10] O. BENDIKSEN, A new approach to computational aeroelasticity, in: *32nd Structures, Structural Dynamics, and Materials Conference*, 1991, p. 939.
- [11] F. Nobile, L. Formaggia, A stability analysis for the arbitrary Lagrangian Eulerian formulation with finite elements, *East-West Journal of Numerical Mathematics* 7 (ARTICLE) (1999) 105–132.
- [12] L. Formaggia, F. Nobile, Stability analysis of second-order time accurate schemes for ALE–FEM, *Computer Methods in Applied Mechanics and Engineering* 193 (39-41) (2004) 4097–4116.
- [13] A. Bonito, I. Kyza, R. H. Nochetto, Time-discrete higher-order ALE formulations: stability, *SIAM Journal on Numerical Analysis* 51 (1) (2013) 577–604.
- [14] D. Boffi, L. Gastaldi, A fictitious domain approach with Lagrange multiplier for fluid-structure interactions, *Numerische Mathematik* 135 (3) (2016) 711–732. doi:10.1007/s00211-016-0814-1.

- 1401
1402
1403
1404
1405
1406
1407
1408
1409
1410
1411
1412
1413
1414
1415
1416
1417
1418
1419
1420
1421
1422
1423
1424
1425
1426
1427
1428
1429
1430
1431
1432
1433
1434
1435
1436
1437
1438
1439
1440
1441
1442
1443
1444
1445
1446
1447
1448
1449
1450
1451
1452
1453
1454
1455
1456
- [15] D. Boffi, N. Cavallini, L. Gastaldi, The finite element immersed boundary method with distributed Lagrange multiplier, *SIAM Journal on Numerical Analysis* 53 (6) (2015) 2584–2604. doi:10.1137/140978399.
- 275 [16] O. Pironneau, Numerical study of a monolithic fluid–structure formulation, in: *Variational Analysis and Aerospace Engineering*, Springer International Publishing, 2016, pp. 401–420. doi:10.1007/978-3-319-45680-5_15.
- [17] Q. Du, M. D. Gunzburger, L. S. Hou, J. Lee, Analysis of a linear fluid-structure interaction problem, *Discrete and Continuous Dynamical Systems* 9 (3) (2003) 633–650.
280
- [18] J. Lequeurre, Existence of strong solutions to a fluid-structure system, *SIAM Journal on Mathematical Analysis* 43 (1) (2011) 389–410.
- 285 [19] C. Grandmont, Y. Maday, Existence for an unsteady fluid-structure interaction problem, *ESAIM: Mathematical Modelling and Numerical Analysis* 34 (3) (2000) 609–636.
- [20] F. Nobile, C. Vergara, An effective fluid-structure interaction formulation for vascular dynamics by generalized Robin conditions, *SIAM Journal on Scientific Computing* 30 (2) (2008) 731–763.
- 290 [21] C.-Y. Chiang, O. Pironneau, T. Sheu, M. Thiriet, Numerical study of a 3d Eulerian monolithic formulation for incompressible fluid-structures systems, *Fluids* 2 (2) (2017) 34.
- [22] T. Belytschko, W. K. Liu, B. Moran, K. Elkhodary, *Nonlinear finite elements for continua and structures.*, John Wiley & Sons, 2013.
- 295 [23] J. R. Magnus, H. Neudecker, *Matrix differential calculus with applications in statistics and econometrics*, John Wiley & Sons, 2019.
- [24] T. Richter, T. Wick, Finite elements for fluid–structure interaction in ALE and fully Eulerian coordinates, *Computer Methods in Applied Mechanics and Engineering* 199 (41-44) (2010) 2633–2642.
- 300 [25] S. Brenner, R. Scott, *The mathematical theory of finite element methods*, Vol. 15, Springer Science & Business Media, 2007.
- [26] J. Nocedal, *Conjugate gradient methods and nonlinear optimization*, *Linear and nonlinear conjugate gradient-related methods* (1996) 9–23.
- [27] R. Glowinski, *Finite element methods for incompressible viscous flow*, *Handbook of numerical analysis* 9 (2003) 3–1176.
- 305 [28] H. C. Elman, D. J. Silvester, A. J. Wathen, *Finite elements and fast iterative solvers: with applications in incompressible fluid dynamics*, Oxford University Press, USA, 2014.

1457
1458
1459
1460
1461
1462
1463
1464
1465
1466
1467
1468
1469
1470
1471
1472
1473
1474
1475
1476
1477
1478
1479
1480
1481
1482
1483
1484
1485
1486
1487
1488
1489
1490
1491
1492
1493
1494
1495
1496
1497
1498
1499
1500
1501
1502
1503
1504
1505
1506
1507
1508
1509
1510
1511
1512

- [29] D. Mitrovic, D. Zubrinic, *Fundamentals of applied functional analysis*, Vol. 91, CRC Press, 1997.
- 310 [30] C. Hesch, A. Gil, A. A. Carreño, J. Bonet, P. Betsch, A mortar approach for fluid–structure interaction problems: Immersed strategies for deformable and rigid bodies, *Computer Methods in Applied Mechanics and Engineering* 278 (2014) 853–882. doi:10.1016/j.cma.2014.06.004.
- 315 [31] O. Pironneau, Numerical study of a monolithic fluid–structure formulation, in: *Variational Analysis and Aerospace Engineering*, Springer, 2016, pp. 401–420.
- [32] S. Turek, J. Hron, Proposal for numerical benchmarking of fluid–structure interaction between an elastic object and laminar incompressible flow, in: *Fluid-Structure Interaction*, Springer, 2006, pp. 371–385.
- 320 [33] L. Zhang, M. Gay, Immersed finite element method for fluid-structure interactions, *Journal of Fluids and Structures* 23 (6) (2007) 839–857. doi:10.1016/j.jfluidstructs.2007.01.001.
- [34] F. Hecht, New development in FreeFem++, *Journal of Numerical Mathematics* 20 (3-4) (2012) 251–265.
325 URL <https://freefem.org/>
- [35] C. Hesch, A. Gil, A. A. Carreno, J. Bonet, P. Betsch, A mortar approach for fluid–structure interaction problems: Immersed strategies for deformable and rigid bodies, *Computer Methods in Applied Mechanics and Engineering* 278 (2014) 853–882.